Sustainable Energy Technologies and Assessments 52 (2022) 102110

Contents lists available at ScienceDirect

Sustainable Energy Technologies and Assessments

journal homepage: www.elsevier.com/locate/seta

Original article

Deep learning-based model for fault classification in solar modules using infrared images

Parsa Haidari [a], Ali Hajiahmad [a,*], Ali Jafari [a], Amin Nasiri [b]

[a] College of Agriculture & Natural Resources, University of Tehran, Iran
[b] Department of Biosystems Engineering and Soil Science, University of Tennessee, Knoxville, TN, USA

ARTICLE INFO

Keywords:
Deep learning
Performance evaluation
Hotspot
Feature map analysis
Fault detection

ABSTRACT

The efforts to decrease air pollutants using renewable energies, especially photovoltaic energy, are developing rapidly worldwide. Photovoltaic powerhouses contain a large number of photovoltaic power generators called photovoltaic modules that must be investigated regularly. However, these modules cannot be investigated with traditional methods because they are time-consuming and life-threatening. In this article, a deep learning algorithm-based method was developed for photovoltaic powerhouse investigation. Two types of defects were studied in photovoltaic powerhouses, namely hotspot, and hot substring. These defects are more frequent in the photovoltaic powerhouse. Datasets used in this work contain thermal images of photovoltaic modules obtained from aerial and terrestrial images. The prepared network was evaluated by some statistical parameters, including F1 score, accuracy, and precision. Finally, the network was classified with a total accuracy of 0.98, and the obtained results were compared with those of other works.

Introduction

Photovoltaic systems

Photovoltaic energy is a kind of renewable energy that is rapidly growing up throughout the world. From 2010 to 2019, photovoltaic systems' installed capacity has grown from 40 GW to 578 GW [1]. Photovoltaic systems are environment-friendly and generate clean electricity without producing air pollutants or greenhouse gases [2]. Despite these benefits, photovoltaic panels in powerhouses are exposed to humid and high-temperature environments that can provide a source of damage or may serve as a hotspot due to partial shading of around objects on the solar panels [3]. Under such conditions, hotspot cells do not contribute to power production [4] and act as a consumer, which is the most common defect in solar cells [5].

Efficiency of photovoltaic systems

The measured efficiency percentage was investigated versus theoretical efficiency (PR) to analyze module performance in the hotspot condition. The results showed that the PR for healthy modules was 83.8%, but in modules with five and more hotspot cells and modules with hot sub-string were 74% and 71.5%, respectively [6]. A hotspot is a defect that cannot be seen with naked eyes and causes performance degradation in the photovoltaic module.

On the other hand, some visible defects such as dust aggregation on the module surface decline the powerhouse's power. In this respect, research in east China showed that the average dust density in a weak (0.644 g/m^2) covering the photovoltaic modules could decrease the output power by 7.4% [7].

Quantitive methods for powerhouse inspection

Some researchers have used quantitative methods (e.g., electrical characteristics analysis) for fault diagnosis in photovoltaic powerhouses [11,12]. However, in such a method, investigators deal with high-voltage tools, and thus they are exposed to life-threatening risks. Moreover, it is very time-insensitive to check the entire powerhouse. Also, electrical analysis in powerhouses may be associated with powerhouse shutting down. Researchers have proposed methods based on imaging inspections when the powerhouse is in operating mode to handle such problems. Imaging inspection is a cost-effective and time-saving method for the fault detection of photovoltaic plants [13]. Imaging inspection of photovoltaic installations is performed in three

* Corresponding author.
E-mail addresses: hajiahmad@ut.ac.ir (A. Hajiahmad), anasiri@utk.edu (A. Nasiri).

https://doi.org/10.1016/j.seta.2022.102110
Received 19 July 2021; Received in revised form 17 February 2022; Accepted 19 February 2022
Available online 25 February 2022

significant ways: electroluminescence image inspection, visible image inspection, and thermal image inspection.

Types of image inspection

Electroluminescence imaging is used to investigate the photovoltaic systems accurately using a high-resolution CCD camera. Although this method works well for defect detection in the photovoltaic cells, it encounters some limitations in the photovoltaic powerhouse for defect detection in photovoltaic modules. In this method, an external power source must be used to excite the photovoltaic module; this, in turn, leads to high energy consumption, and it needs professional knowledge for the proper setup. Also, this method is time-consuming, and it needs some operators to change the setup position [14].

Visible degradation phenomenon can be categorized into three types: The first type is module components failure, which can be seen in any part of the module (e.g., cracks in the module glass or damage to the insulation section which cause influence dust and moisture to solar modules). The second type is module delamination, which is observed on both sides of photovoltaic modules and disrupts sunlight to reach solar cells. The third one is moisture influence, affecting the rusty solar modules and cause corrosion in electrical connections [8]. Discoloration in photovoltaic modules is a type of visible degradation that is created by high temperatures. In a study in Morocco, this phenomenon caused a 5.28% power reduction in terms of the maximum output power [9]. All of these problems cause performance degradation in photovoltaic powerhouses. Therefore, the performance of installed photovoltaic powerhouses highly depends on periodic inspection and maintenance. For this purpose, a fast and reliable defect detection approach has particular importance for protecting the photovoltaic system and deriving optimum output power from solar panels [10].

In the visible imaging method, only visible faults that are recognized with human eyes can be checked. Such as snail trails and dust accumulation on the module surface. It is of note that maybe some defects not be considered in this technique. Furthermore, the defects that cause a change in temperature distribution are critical and influence the module performance. Some visible defects may appear on the module surface, but they do not significantly disrupt the module function.

Thermal imaging is more effective than visible and electroluminescence imaging because it can present an abnormal temperature pattern of defected solar modules and detect more faults in the photovoltaic inspection process [15]. Thermal imaging is performed with a thermal camera that can detect wavelengths from 8 to 14 μm. Some methods have been developed to help abnormalities detection using thermal images based on image processing techniques, fuzzy rule-based techniques, and machine learning-based algorithms.

Traditional imaging-based methods for fault inspection

A Canny edge detector was used for fault detection in some pv modules in the image processing technique. In this method, after capturing images with a thermal camera, a threshold obtained with trial and error was applied to background segmentation. Then, the image was fed to the Canny edge detector to recognize hotspot regions and count them. Experimental results showed that the technique recognized 13 cells from 14 defective cells. Also, in the presented research, a method based on temperature line analysis could easily highlight the hotspots [16]. The main disadvantage of this technique was choosing fixed numbers for the threshold task. Because of the change in the module environment, the image intensity was changed accordingly, and the fixed threshold cannot perform the separation task well. Also, as mentioned by the authors, some small defective points might not be considered in the photovoltaic module.

For noise reduction in thermal images and distinguishing the hotspots, a technique based on curve fitting and peak detection in the thermal image histogram was performed. In this approach, the threshold was obtained automatically to segment the hotspots from the background [17]. This technique was carried out on a photovoltaic module with a specific condition and needed more samples to evaluate the performance.

In fuzzy rule-based techniques, images were resized to a specific size for comparison. A healthy module was taken as a reference, and other modules were compared with this module in the color pattern and pixels intensity. According to this comparison and photovoltaic modules' working temperature, the module's images were categorized into five defective levels from no fault to critical fault [18]. This technique needed high accuracy on image cropping because it can affect comparison results and change the degree of defect. Also, the results of this technique were highly correlated with the principle module and changed with the other principles. Besides, the technique will work on the modules with match specifications and the same condition.

Neural network-based methods

Machine learning algorithms based on artificial neural networks (ANNs) and DNNs have been employed for fault detection in photovoltaic systems. For defect detection or classification with ANNs, researchers extract features like image contrast, entropy, and homogeneity [19] from the thermal images manually and train the network. This process is time-intensive and may not extract all effective features from the image. Besides, in this method, the model's behavior on features cannot be surveilled. Some numerical features can be extracted from images that do not correlate with the main object, and the module environment or condition influences their value. Especially, some images taken in different conditions (e.g., various sun intensities during the day and different orientations of the defect in the photovoltaic modules) can be fed into the network. Besides, DNN's abilities contribute to solving these problems and enhancing the classifier performance. These networks extract effective features from thermal images automatically and provide better performance [20]. Convolution neural networks (CNNs) are a subset of DNNs that have some layers with a partial connection of neurons to the next layer. Such an architecture can speed up the processing operations for automatic feature extraction. These layers have some advantages, such as the local relationship between units and not being affected by scale changing [21].

Regarding the advantages of CNN in automatic and efficient feature learning, some DNN-based algorithms have been developed to find the fault in photovoltaic systems. For instance, a region-based CNN was designed for detecting the defects in the thermal images taken up with UAV. This approach could detect the defect regions with an accuracy of 99.02% and precision of 91.67% [22]. However, the low precision in the hot region detection caused time consumption and made a false alarm. Also, changes in the module environment might influence module detection, and the different environmental conditions might affect the model performance. In another study, the VGG16 CNN network was used for automatic defect detection in the photovoltaic plant images. Precision and F1 score of this architecture with data augmentation technique were obtained to be 0.76 and 0.75, respectively [23]. This method is described further in the last part of this paper (Section "Results and discussion").

Five CNN models were developed with different architectures to distinguish between the hotspot and dust in the photovoltaic modules. The results showed that the model with more layers had the best results. The dataset prepared for this model contained the images processed by a combination of Box Blur and Sobel-Feldman filters. Eventually, the classification task was performed with an accuracy of 98% [24]. Although this study showed high performance in classification tasks, dust accumulation might create hotspot conditions [25], and these two defects were not wholly separable from each other. It is of note that hotspot detection may suffice the defect detection in the powerhouse. Also, dust accumulation in the photovoltaic modules could be detected by the naked eye and did not need high price equipment such as a

thermal camera.

UAVs imaging-based methods

UAVs for photovoltaic powerhouse inspection, which is equipped with a thermal camera, were proposed for faster inspection. Although this technique was time-saving, it needed high-resolution thermal cameras and UAVs, which might not be economically justified for all powerhouses with a different scale. Moreover, the technique did not have enough precision to replace the close-distance human inspection [26,27]. Meanwhile, automatic defect detection in UAV-based methods strongly corresponded to the module detection in photovoltaic powerhouses. Besides, if photovoltaic modules arrangement were changed in some other powerhouses, the task may fail. A study conducted on the module and defect detection with UAVs F1 scores of 0.8 and 0.81 were obtained, respectively [28]. So, some of the modules were not detected in this work due to the low accuracy, which may increase the risk of defect expansion and creating a significant failure in the powerhouse.

Two types of common defects in photovoltaic powerhouses were evaluated in this study. Hotspot and hot substring were two types of module failure that were chosen for abundant investigation in the photovoltaic powerhouse. In a Japanese study, 1,272 photovoltaic modules were evaluated, of which 593 modules had the bypass diode defects that a reason for hot substring failure [29–31] In another study, 17,142 modules were investigated, of which 859 modules were defective due to the hotspot, and 123 modules were damaged in the bypass circuit [32]. Also, these defects might cause fire more than other defects in photovoltaic powerhouses due to the high temperatures produced by them [30,33].

Current study approach

In spite of the significant results of deep learning-based models, the used datasets consist of powerhouse images with the same environmental parameters, which may cause false alarms in other powerhouses' environmental conditions. Accordingly, the current study aimed to diagnose photovoltaic modules' fault diagnosis using thermal images obtained from different photovoltaic powerhouses taken by UAV or human portable cameras. To this end, the VGG16 architecture was modified in accordance with the current study's goals to obtain a comprehensive model for defect detection in photovoltaic powerhouses. The study's dataset was collected from various powerhouses worldwide under different conditions. Therefore, the dataset had proper distribution in terms of different irradiation, imaging heights and angle, various environment temperatures, different weather conditions, and times used for data collection. The following section describes a) dataset preparation and image preprocessing techniques from polycrystalline photovoltaic modules, b) the specification of purposed architecture and the reason for choosing VGG16 architecture, and c) model evaluation methods.

Material and methods

In the present study, two common defects were analyzed in photovoltaic powerhouse modules based on deep learning-based methods using thermography images. The dataset included UAV and manual inspection images from various powerhouses around the world. The CNN VGG16 architecture was selected for classification tasks because of its comprehensiveness and efficiency in classification tasks [34] and defect detection in photovoltaic modules [35]. This architecture was created by the Visual Geometry Group (VGG) at Oxford University [36], and it was trained on the ImageNet database (containing 3.2 million images with full resolution) for a classification task. The transfer learning technique was used to reduce processing operations in the VGG16 architecture employed in this work, and then the modified fully-connected layers of VGG16 architecture were trained. The transfer learning technique was performed by training the network on other datasets and learning some general features that could deal with any dataset, and helping the network learn more efficient encounters with new datasets [37].

Database preparation

To train the CNN model, first, the databases were prepared by combining thermal images obtained from photovoltaic powerhouses taken by UAV or human's portable cameras from a near distance. Thermal images were collected using images collection of research sources [55]. For quality improvement, the Median Blurring image-processing technique was used as well. The techniques eliminated undesirable noise in the images and around the image boxes created in the cropping process. All properties from digital images were needed for defect detection. Therefore, after quality enhancement, all images were converted to grayscale color space to make a uniform dataset. Finally, all panels were manually cropped from thermal images using Adobe Photoshop software to obtain a high-quality dataset. Fig. 1 presents the process of extracting photovoltaic module images from thermal images [38]. Some powerhouse modules junction boxes were shining in thermal images, and others not. Since it was not an inherent defect in the photovoltaic module, for the sake of data homogenization, the shiny junction boxes were manually eliminated by image cropping in all images. Two types of common defects [5] in photovoltaic powerhouses were prepared for the classification task. Thus, the proposed dataset had three classes (including healthy, hotspot, and hot substring) collected in the photovoltaic powerhouse. In general, 1,116 images were manually labled for the classification task, including 200 hotspots, 200 hot substrings, and 716 health modules [39]. In the presented dataset, some modules might contain several hotspots or hot substring.

Purposed VGG16 architecture

In this study, a modified VGG16 was used for fault classification in a photovoltaic module. The VGG16 network, which Simonyan and Zisserman developed, consisted of 13 convolution layers in five blocks. Each block was followed by a MaxPooling layer in this system and three fully-connected layers [36]. It provided better operation for feature learning compared to structures with a lower number of convolution layers [40]. Channel numbers extracted in initial convolution layers of VGG16 architecture were small and increased gradually from 64 to 512 channels. To increase non-linearity and improve this structure's decision ability, the small size of convolution kernels was substituted in each block of the network without any MaxPooling layers among the blocks instead of large convolution kernels that increased total parameters.

Also, in VGG 16 architecture, odd number filters were used to traverse the input images and made the feature maps. Besides, the output of each convolution layer was crossed the ReLU activation function. In the original structure of the VGG16 network, convolution layers were followed by three fully connected layers with 4096, 4096, and 1000 parameters, respectively. The last layer of the network was equipped with a Softmax activation function for classification tasks [41]. Two advantages of the network that led to considerable success were using the significant deep structure and small filter size in convolution layers. To form the modified structure of VGG16, original fully connected layers were substituted with four low parameters fully-connected layers. Four of the fully connected layers were used for the learning process with 32, 32, 16, and 3 parameters, respectively, and the last one was used for the classification task with Softmax activation function and three outputs. The structure of the final model is presented in Fig. 2. Feature maps were obtained from the feature extractor unit (five blocks) of VGG16, and they were converted to flatten data to feed fully connected layers. After the first dense layer, a dropout layer was employed to prevent the network overtraining. Table 1 is represented the output size of each layer as (height × width × depth) in purposed architecture.

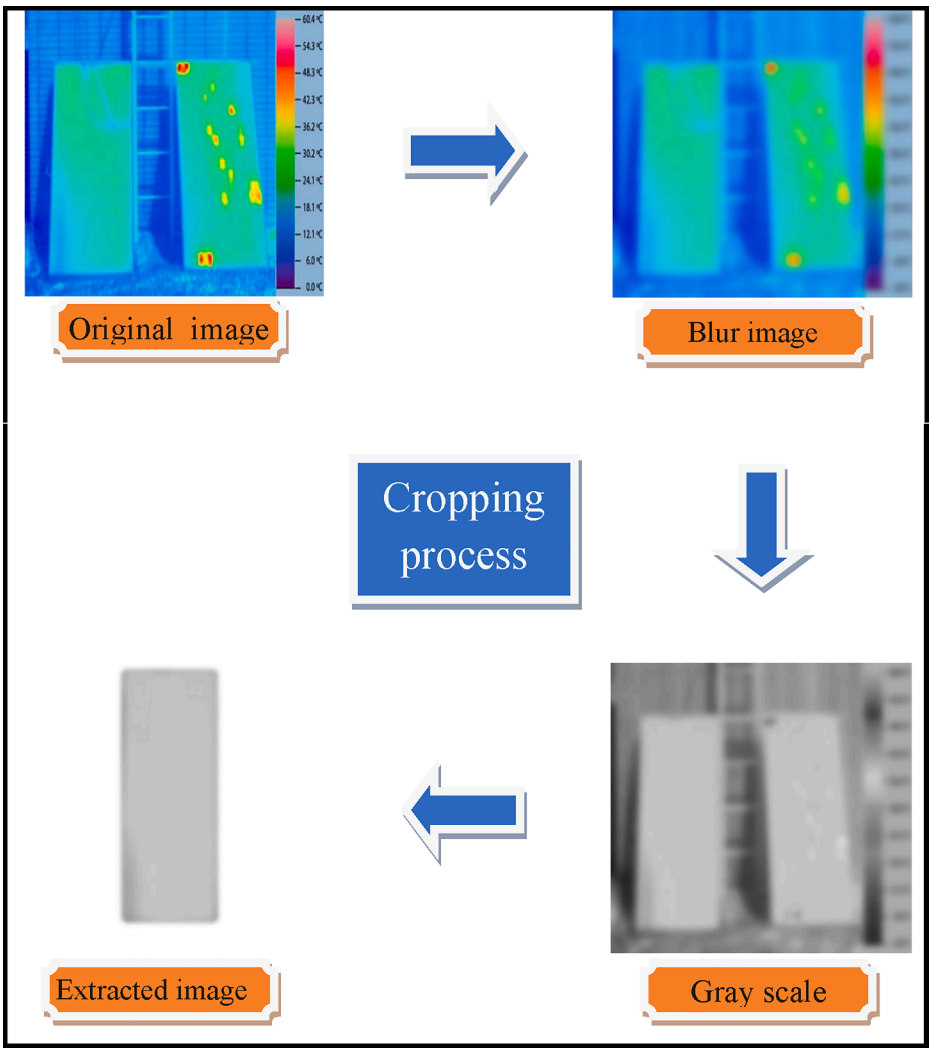

Fig. 1. Photovoltaic module extraction from thermal images process [38].

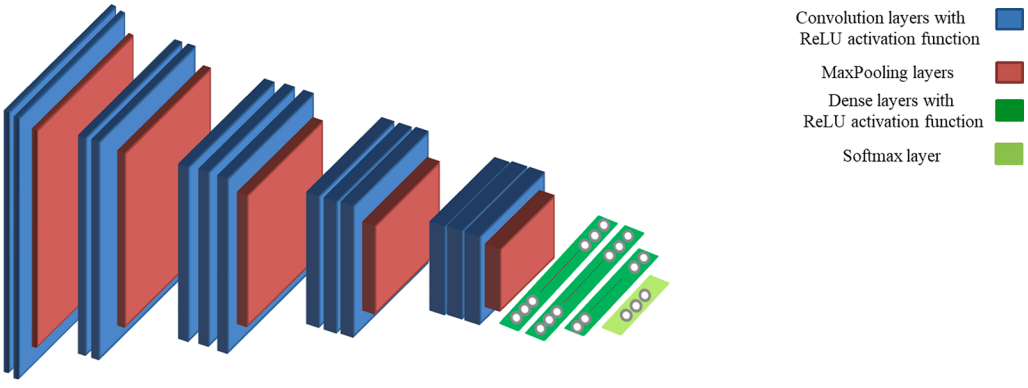

Fig. 2. Architecture of purposed VGG16-based model.

Convolution layer

To extract and learn features from input images, convolution layers with hierarchical arrangement were organized. Features were extracted from images according to the size and amount of convolution kernels. Kernels contained learnable parameters with an adjustable size that were set in the learning process stepwise according to the amount of loss function. Math operation in a convolution layer with a 1×1 kernel size can be expressed as a relation (1):

$$y = f(w \times x + b) \tag{1}$$

where x and y represent the input and output of the layer, w is a learning parameter that can change in the learning process, and b is constant.

Kernels traversed all over the images and extracted a feature map (an image based on the output in relation 1) from input images in each layer. These feature maps in the early layers extracted elementary features like shape boundary, and thus they were more complicated in the last layers

Table 1
Output size of each layer for purposed model.

Layer	Block1	Block2	Block3	Block4	Block5
Convoloution1	70 × 50 × 64	35 × 25 × 128	17 × 12 × 256	8 × 6 × 512	4 × 3 × 512
Convoloution2	70 × 50 × 64	35 × 25 × 128	17 × 12 × 256	8 × 6 × 512	4 × 3 × 512
Convoloution3	–	–	17 × 12 × 256	8 × 6 × 512	4 × 3 × 512
MaxPooling	35 × 25 × 64	17 × 12 × 128	8 × 6 × 256	4 × 3 × 512	2 × 1 × 512
Dense Layers	Dense1 32	Dropout –	Dense2 32	Dense3 16	Softmax 3

[40]. The main idea of CNNs is to construct a hierarchy of self-learned features, which means low-level features (e.g., color and edges) are encoded by the first layers' filters. The filters from the middle convolutional layer encode simple textures constructed from compositions of colors and edges. Filters of the final convolutional layers extract the textures and specific patterns of the images. Thus, higher-level features are built on the low-level ones, and in this way, CNN is capable of constructing robust features.

Max pooling layer

By applying this layer to an input image, pixels with higher values related to their neighbors were kept, and the other ones were constrained. This method caused an image dimension to decrease, which resulted in reducing the superfluous computation. Also, the number of neighbors in the computation was adjusted by setting the kernel size [42].

Fully connected layer

Fully connected layers were chosen as the last layers of the network. All the neurons in the mentioned layers were connected and were employed to learn extracted features from previous layers for intended action [43].

Dropout layer

A layer for parameter regularization was used in a network called the dropout layer to overcome network overfitting. The training process randomly deletes some units by displacing their weights to zero based on a simple mechanism. The dropout approach forces the network to continue the learning process with the remaining weights, leading to learning more features. This mechanism prevents model adaptation to data in the training process, improves model accuracy on test data, and causes significantly lower generalization error on classification problems [42]. The dropout mechanism is presented in Fig. 3.

Activation function

For fully connected layers, ReLU activation functions were used. The ReLU activation function was employed in deep learning networks because of its simple learning strategy. It performed like a threshold function for each negative value and set them to 0 (1). Using this structure improved the effectiveness of the descending gradient problem in the earlier activation function. Moreover, using the ReLU activation function reduced the total computational cost and accelerated the convergence speed since it did not estimate exponentials and divisions [44]. Fig. 4. is presented the chart of the ReLU function. Here, x is defined as the input value of the function.

$$f(x) = \max(0, x) = \begin{cases} x_i, if x_i \geq 0 \\ 0, if x_i < 0 \end{cases} \quad (1)$$

The Softmax (Eq. (3)) activation function was used in the last network layer. This function was developed so that all of its outputs formed probability distribution in the range of 0 and 1, with the sum of 1. The Softmax activation function is widely used in DNNs for multi-variate classification tasks [45].

$$f(x) = \frac{e^{x_i}}{\sum_j^n e^{x_j}} \quad (2)$$

Loss function

The cross-entropy function was used for loss measurement in the multi-classification task. The parameters of this function are represented by relation (3). To correct class detection in the cross-entropy method, the value of this function should be reduced. The total loss value was obtained by calculating the mean loss overall database samples (relation 4) [42].

$$Q_i = -\log(f(x)) \quad (3)$$

$$Q = \frac{1}{N}\sum_{i=1}^{N} Q_i \quad (4)$$

Optimization algorithm

Adam's optimization algorithm was chosen to suppress loss function magnitude because of its higher speed than Stochastic Gradient Descent and the ability to effectively restraining the fluctuations to achive the optimum loss. Moreover, it adds to the advantages of AdaGrad and RMSprop optimization techniques to achieve high-performance. Adam's weight updating strategy is expressed by relations (5), (6), and (7) [46,47].

$$m(w,t) = \gamma_1 m(w,t-1) + (1-\gamma_1)(\nabla Q_i(w)) \quad (5)$$

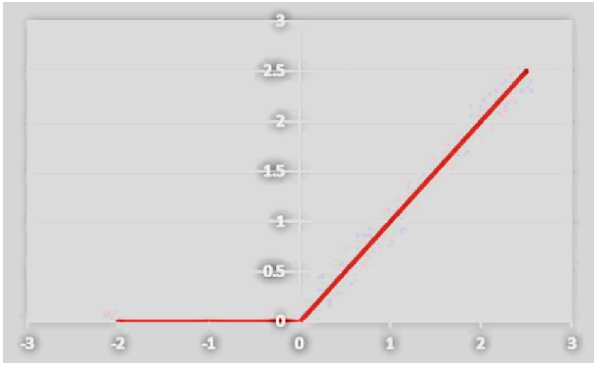

Fig. 4. Linear behavior of ReLU.

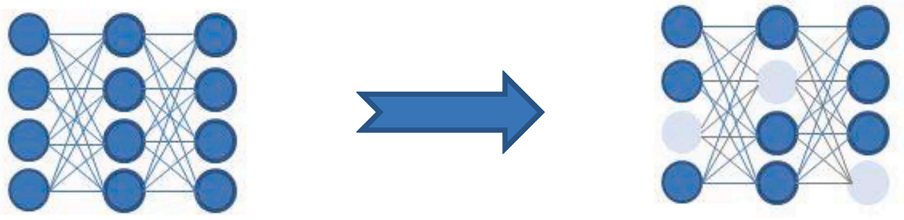

Fig. 3. Mechanism of dropout layers on fully-connected neurons.

$$v(w,t) = \gamma_2 v(w,t-1) + (1-\gamma_2)(\nabla Q_i(w))^2 \quad (6)$$

$$w_{t+1} = w_t - \frac{\eta}{\sqrt{v(w,t)} + \varepsilon} m(w,t).\frac{\sqrt{1-\gamma_2'}}{1-\gamma_1'} \quad (7)$$

where γ_1 and γ_2 are the forgetting factor parameters, w and $\nabla Q_i(w)$ are the weight and loss function gradient, respectively, and $m(w,t)$ and $v(w,t)$ are first and second approximations of gradient moment, respectively.

Fine-Tuning the network

First, randomized data were reconstructed from the original dataset and then were divided into the train (85%) and test data (15%). Also, 20% of the training dataset was set aside for cross-validation. The model was trained with 50 epochs and a batch size of 64. all of the pictures in the dataset were converted to smaller images (70 × 50) to enhance the training speed. A learning rate of 0.001 was chosen to train the model as high learning rate values might disrupt the training process and cause the model captivity in local minima [48]. The decay rate for the Adam optimizer's first and second moments was set to 0.9 and 0.999, respectively. All of the trainable parameters of convolution layers in VGG16 architecture trained on the ImageNet database were frozen and did not contribute to the training process. It is noteworthy that all fully connected layers were free to set in the training process. The dropout technique was employed in this network to prevent the model from memorizing the training data, and the best dropout rate was obtained by trial and error based on model performance and duration of training time.

Evaluation methods

A confusion matrix was provided as a table with some information about the classifier model. In Fig. 5, a 2 × 2 confusion matrix shows the model predicted classes against true ground classes. In this method, model performance was evaluated based on the data represented in each block. If all numbers placed on major diagonal and sub-diagonal blocks were 0, an optimal mode for confusion matrix was made, and model accuracy was reached the high value. It means that the whole model prediction was accurate [49].

In the major diagonal of the matrix shown in Fig. 5, TP represents correct objects that the model predicts in the correct class and TN represents false objects that the model predicts correctly in a false class. In the sub-diagonal, FN represents proper objects that the model verifies wrongly as false objects, and FP represents false objects that the model verifies wrongly in the proper class.

In this study, standard model evaluation methods such as accuracy, precision [50], sensitivity, recall, and F1 score were calculated for a comprehensive checking of the result. F1 score was chosen and obtained by calculating the harmonic mean of precision and recall metrics functions because of its importance compared to the model results to find the best model parameters (Table 2) [51]. Precision was chosen as a criterion to show how many samples that the model had predicted as a proper class were delusive. Sensitivity was selected as a criterion to specify the number of proper classes that were predicted as wrong classes. Also, accuracy was chosen to have a general view of model performance.

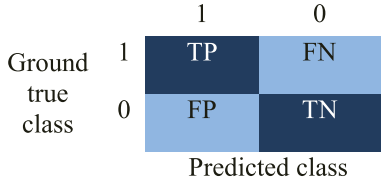

Fig. 5. Confusion matrix.

The model was trained using a computer with a Core i7 CPU with 3.5 GHz speeds and 8 GB of RAM running on the Windows 10 operating system.

Results and discussion

Model training and validation of accuracy and loss for 50 epochs are presented in Fig. 6. According to the best accuracy and loss values, the optimum epoch for model training and cross-validation was obtained in Epoch 44. On average, the training time for each epoch was 25 s. Total model accuracy and loss in Epoch 44 were obtained at 0.98 and 0.12 for test results, respectively. These results showed the high performance of VGG16 deep hierarchical architecture in feature extraction and classification task. The dropout parameter was set by trial and error, and it helped the network to converge rapidly. Different dropout values were examined, and the value of 0.15 had the best performance for this network in Epoch 44. Without the dropout layer, more than 50 epochs were needed for network convergence.

The model confusion matrix is presented in Fig. 7. As can be observed, most incorrect predictions belonged to the hotspot class. This class had two incorrect predictions that were recognized as a healthy module. It probably occurred due to network sensitivity for the hotspot dimension. Since the hotspots had different dimensions in images, they might be minimal and not considered by the network. One healthy module was classified in hotspot class. This problem might occur due to the shiny surface of the solar module under bright sunlight or a high gap between cells that eliminated temperature distribution uniformity on the module surface; however, in reality, this module was healthy. Also, one hot substring module was predicted as a healthy module that could have occurred due to low substring intensity concerning the whole module surface. As shown in Table 3, average values of accuracy, precision, sensitivity, specificity, negative predictive value, and F1 score for three classes were 0.98, 0.98, 0.97, 0.98, 0.99, and 0.98, respectively.

The average negative predictive value for the present work was 0.99, indicating the model reliability to extract defect modules (all of them were damaged).

Since the model showed high reliability in powerhouse investigation and almost no healthy modules were eliminated from powerhouse wrongly, the investigated powerhouse owners can rely on the model judgments and change the defective modules without any concern about losses to increase the powerhouse performance.

To better understand the network's learning process, 16 feature maps from convolution layers located before network pooling layers were selected. These feature maps are shown in Fig. 8.

As can be seen from Fig. 8, the extracted initial feature maps contained many features and were more like the original module pictures, but as the network reached close to the last layers, these features lost more of the original shapes. The process showed that the top layers were extracted features that specify defect shape and size. However, the last layers feature maps that were shaped by convolution kernels scanned the whole image to find defects everywhere in the image (invariant property of convolution layers) [52]. In healthy modules, active points were similar to continuous halation areas with different shapes or areas that randomly surrounded some feature maps. Substring defect modules, active points were similar to strip regions that corresponded to substring defect. In modules with hotspot defect, horizontal or vertical strip bar could be seen, but a point in these regions was brighter than the others, and the brightness was gradually distributed in the activation area. However, in the last layers, the feature maps for healthy and hotspot modules became more similar. In the 17th convolution layer, feature maps were more like a coding system that only the network can deal with.

Due to the different solar radiation in images and network results, the model can learn some independent features of solar radiation levels to detect hot areas, and radiation levels did not significantly affect fault detection in photovoltaic modules. It can occur because the studied

Table 2
Statistical parameter of confusion matrix formula.

Accuracy	Precision	Sensitivity	Specificity	Negative predictive value (NPV)	F1
$\frac{TP+TN}{TP+FP+TN+FN}$	$\frac{TP}{TP+FP}$	$\frac{TP}{TP+FN}$	$\frac{TN}{TN+FP}$	$\frac{TN}{TN+FN}$	$\frac{2\times TP}{2\times(TP)+(FP)+(FN)}$

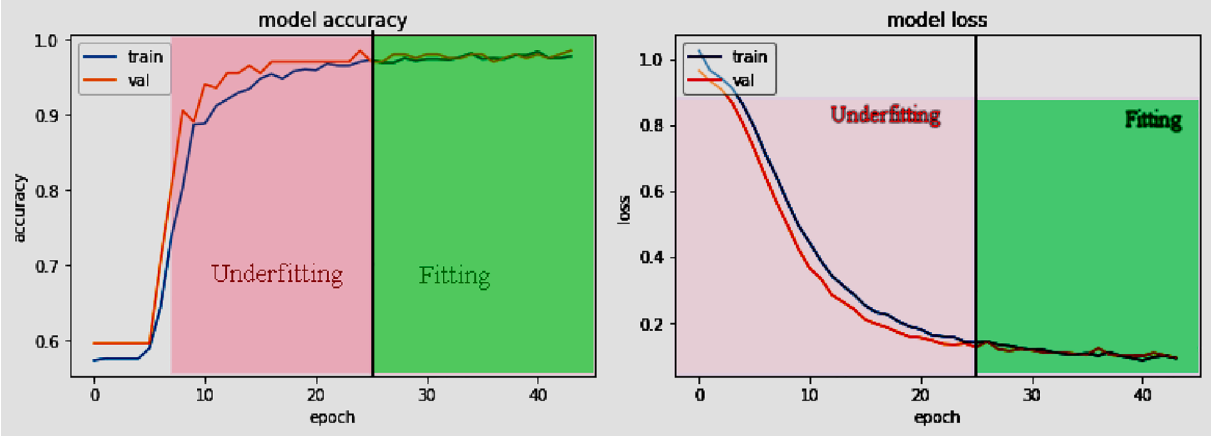

Fig. 6. Classification accuracy (left figure) and cross-entropy loss (Right figure).

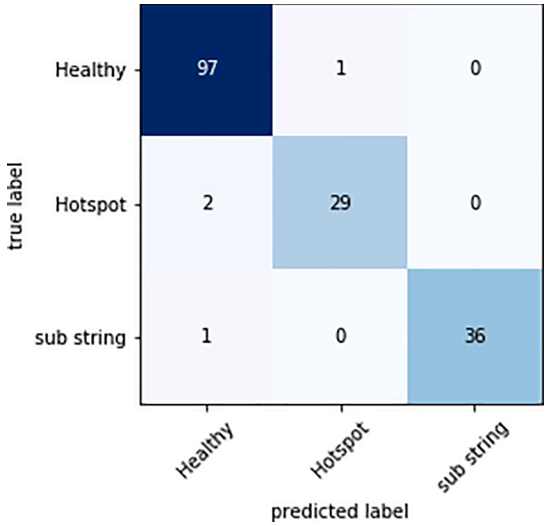

Fig. 7. Confusion matrix for VGG16 network on internet dataset.

defects had a high temperature in any sun irradiation. It did not matter whether the photovoltaic modules' surface was very bright in high light intensities or low bright in low-level sun irradiation; hotspots were a kind of defect and had enough power for consumption. They remained brighter than the whole surface module. Hot areas converted partial available power by themselves to the heat. Therefore, hotspots still appeared brighter than the whole module's surface due to the failure in the cells and consumption power as heat. In this regard, since the brightness of hotspots and hot substrings compared to the surface of the whole module had already been studied [53], the network detected the edges of these defects in photovoltaic modules. As shown in Fig. 8, features extracted by initial convolution layers showed that the network paid more attention to the high-intensity parts of the pictures. It is shown that the network could do the judgment in different levels of light intensity because hotspots and hot substrings were the brightest points in the images.

Additionally, the last feature maps of the network considered local patterns from images, such as changes in intensity levels from pixel line to another pixel line, forming an edge; it means detecting faults in the modules. It is of note that the model was sensitive to sudden changes in the module's surface brightness. However, very low sun intensities might reduce module power production, leading to the hotspot and hot substring boundaries' disappearance. This condition might decline the network performance.

Furthermore, the network was trained by images captured on different distances with different resolutions. Distance and resolution, as two crucial imaging parameters, may affect the network predictions and feature extraction. When the network was trained by near-distance images taken with a high-resolution thermal camera, some of the defects would not be recognized by the network in the far images. The reason is that far images had a different scale with low details, and defects were seen like halation area in module's surface, making the defects recognition hard. Otherwise, if the training images included far distance images with a low-resolution camera, some extracted features from the image may disrupt the network reorganization for near distance images. For example, in near distance images of photovoltaic modules, more details such as a long gap between cells (non-uniform temperature distribution) and highlighted cell boundaries may be recognized as hot substring or hotspot edges. Hence, the distance from modules and camera-resolution might affect the network verification. Cell distances

Table 3
Statistical indicators for VGG16 classification network.

Classes	Accuracy	Precision	Sensitivity	Specificity	negative predictive value	F1 score	Total number
0	0.98	0.97	0.99	0.96	0.98	0.98	98
1	0.98	0.97	0.94	0.99	0.99	0.95	31
2	0.99	1	0.97	1	0.99	0.99	37
Average for each class	0.98	0.98	0.97	0.98	0.99	0.98	

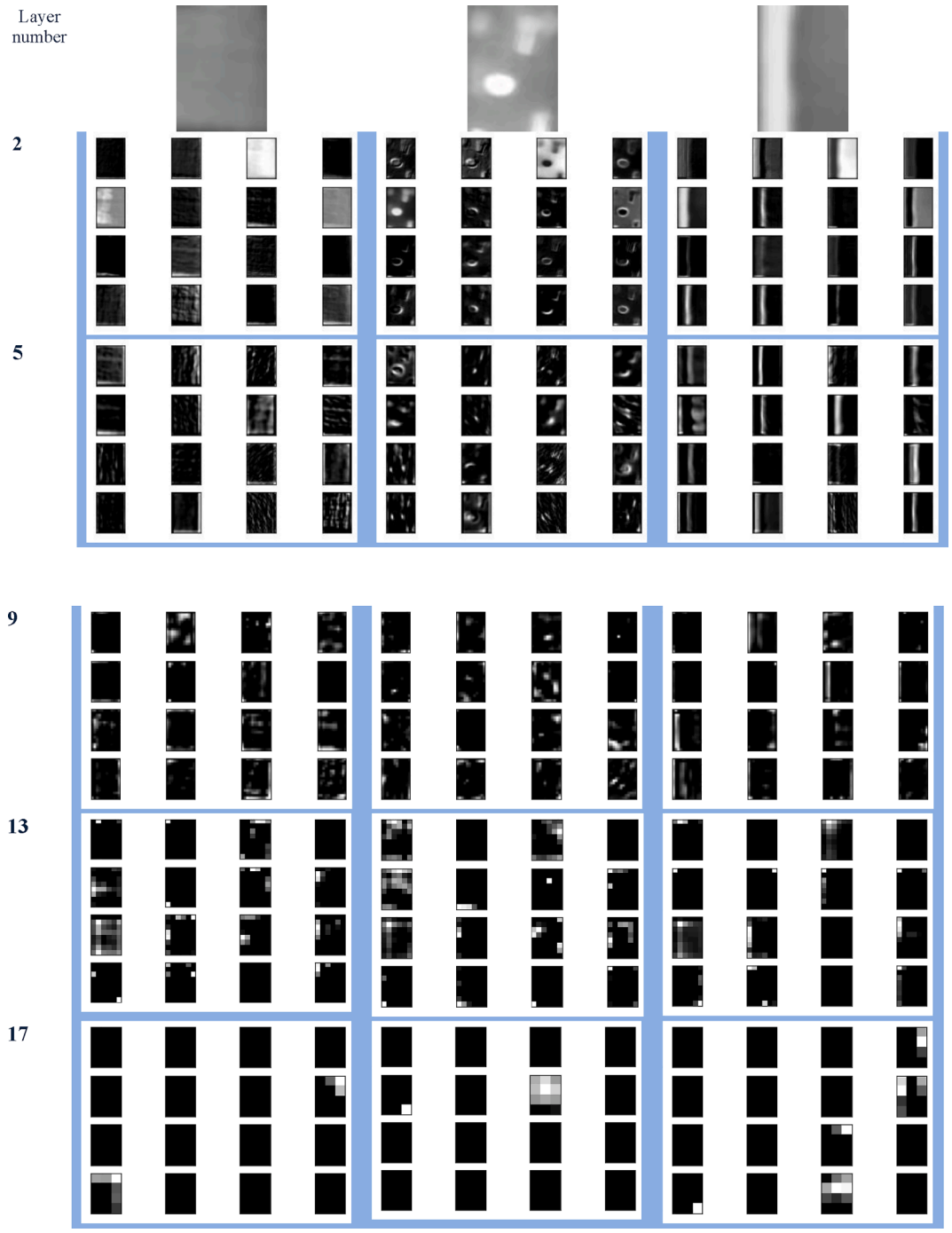

Fig. 8. Some extracted feature maps from healthy (The left column), hotspot (Middle column) and hot substring (Right column) modules. Each column represents the feature maps of different layers according to the hierarchical structure of CNN model.

were more noticeable, mainly when different factories produced modules. According to the test results, the developed network was trained very well, and it overcame these problems through employing the automatic feature extraction from the rich dataset and using the VGG16 pre-trained model on CNNs territory.

Image processing techniques were used for fault detection in 1,544 photovoltaic modules in 37 thermography images. Four steps were used for module detection and segmentation: temperature normalization, automatic thresholding, orientation detection, and final image repairing. After that, modules were analyzed, and defective modules were categorized as defective modules, defective substring, and defective cells. Eventually, the F1 score for module detection and module analysis were 92% and 93%, respectively. Module detection and module analysis showed a low precision of 88 and 90%, respectively [54], probably due to using fixed numbers suitable for a lot of modules or defects, but not for all of them. Also, the selected features were probably not efficient enough to detect photovoltaic modules and corresponding defects.

Nevertheless, the F1 score was improved in the defects classification by using the presented deep neural network compared to the image processing technique method. Furthermore, the image processing technique had a complex pipeline for module segmentation and feature extraction for module analysis. Because pictures prepared for modules evaluation had enough distance to each other because of the specific range of angle imaging, these conditions could be observed in not all

photovoltaic powerhouses. Module arrays might have different arrangements: for example, some modules are mounted on top of each other. Moreover, in the module segmentation process, some constant values were used that might not work in different conditions and cause accuracy dropping.

Pierdicca et al. applied the VGG16 architecture for fault detection in the photovoltaic powerhouse. According to the results, the balanced dataset used in the augmentation techniques contained 6,488 images and had the best F1 score (0.75) for two classes with accuracy of (0.73). As one reason for the low F1 score, most of the Pierdicca network faults recognized as damaged cells in the photovoltaic powerhouse were healthy. However, in the current study, three classes studied with pre-trained VGG16 using the modified fully connected layers showed improvement in the F1 score [23].

In another method, pre-trained VGG16 was used for feature extraction and Faster RCNN for image fault detection. F1 score of this method was 0.95 with accuracy of 0.99 [55].

The results of this model were correlated with the height of the imaging, and maybe some of the defective modules have not been considered due to low-resolution images. Also, in aerial imaging, the reflection area can cause trouble more than terrestrial imaging to find a good position. Imaging under unfavorable atmospheric conditions or windy days can affect the image recording process and make modules hard to examine [56]. However, in our method, more defects with different sources were studied, allowing more accurate programming for powerhouses. Because of containing different powerhouse modules, the dataset used in this study increased network comprehensiveness. The reason is that images were different in this dataset, even for each class. More statistical results presented in this study for model evaluation can lead to better model evaluation. Also, model performance was increased using modified pre-trained VGG16 compared to other aerial methods with simple network structures [57]. The model presented in this work, because of using the pre-trained model and comprehensive dataset, had high performance such that it can be employed on other powerhouses for fault detection with high accuracy.

Conclusion

Quick fault diagnoses in photovoltaic powerhouses are significant to continue working with high efficiency and without risk of intense damage. Using a simple deep learning-based method for fault diagnosis in this study revealed the high efficiency and ability of DNNs on photovoltaic thermal image classification. For this purpose, VGG16 architecture with modified fully connected layers was applied for classification tasks using the transfer learning technique. Two defects (i.e., hotspot and hot substring) observed in a photovoltaic powerhouse with high frequency were investigated. The results showed that this architecture could distinguish between these defects and healthy modules with high total accuracy of 0.98. A noteworthy advantage of this system is that it can be employed on an android portable device for ease of investigation and making this system available to all powerhouse owners.

CRediT authorship contribution statement

Parsa Haidari: Software, Writing – original draft, Visualization. **Ali Hajiahmad:** Validation, Investigation, Writing – original draft, Project administration, Resources. **Ali Jafari:** Conceptualization, Methodology, Resources, Writing – review & editing. **Amin Nasiri:** Resources, Investigation, Writing – review & editing.

Declaration of Competing Interest

The authors declare that they have no known competing financial interests or personal relationships that could have appeared to influence the work reported in this paper.

Acknowledgement

This research did not receive any specific grant from funding agencies in the public, commercial, or not-for-profit sectors.

References

[1] Solar energy n.d. https://www.irena.org/solar (accessed March 3, 2021).
[2] Jiménez-Torres M, Rus-Casas C, Lemus-Zúñiga LG, Hontoria L. The importance of accurate solar data for designing solar photovoltaic systems-Case studies in Spain. Sustain 2017;9:247. https://doi.org/10.3390/su9020247.
[3] Larue JC, du Trieu E. Effect of partial shadowing on solar panels hot spot or breakdown?. In: Comm. Eur. Communities, EUR, D. Reidel Publ Co; 1981. p. 490–5. https://doi.org/10.1007/978-94-009-8423-3_72.
[4] Ahsan S, Niazi KAK, Khan HA, Yang Y. Hotspots and performance evaluation of crystalline-silicon and thin-film photovoltaic modules. Microelectron Reliab 2018; 88–90:1014–8. https://doi.org/10.1016/j.microrel.2018.06.097.
[5] Gallardo-Saavedra S, Hernández-Callejo L, Duque-Perez O. Analysis and characterization of PV module defects by thermographic inspection. Rev Fac Ing Univ Antioquia 2019:92–104. https://doi.org/10.17533/udea.redin.20190517.
[6] Dhimish M, Mather P, Holmes V. Evaluating Power Loss and Performance Ratio of Hot-Spotted Photovoltaic Modules. IEEE Trans Electron Devices 2018;65(12): 5419–27. https://doi.org/10.1109/TED.2018.2877806.
[7] Chen J, Pan G, Ouyang J, Ma J, Fu L, Zhang L. Study on impacts of dust accumulation and rainfall on PV power reduction in East China. Energy 2020;194: 116915. https://doi.org/10.1016/j.energy.2020.116915.
[8] Quintana MA, King DL, McMahon TJ, Osterwald CR. Commonly observed degradation in field-aged photovoltaic modules. In: Conf. Rec. IEEE Photovolt. Spec. Conf.; 2002. p. 1436–9. https://doi.org/10.1109/pvsc.2002.1190879.
[9] Bouaichi A, Merrouni AA, El Hassani A, Naimi Z, Ikken B, Ghennioui A, et al. Experimental evaluation of the discoloration effect on PV-modules performance drop. Energy Procedia 2017;119:818–27.
[10] Du B, He Y, He Y, Duan J, Zhang Y. Intelligent Classification of Silicon Photovoltaic Cell Defects Based on Eddy Current Thermography and Convolution Neural Network. IEEE Trans Ind Informatics 2020;16(10):6242–51. https://doi.org/10.1109/TII.2019.2952261.
[11] Bressan M, El Basri Y, Galeano AG, Alonso C. A shadow fault detection method based on the standard error analysis of I-V curves. Renew Energy 2016;99: 1181–90. https://doi.org/10.1016/j.renene.2016.08.028.
[12] Fadhel S, Delpha C, Diallo D, Bahri I, Migan A, Trabelsi M, et al. PV shading fault detection and classification based on I-V curve using principal component analysis: Application to isolated PV system. Sol Energy 2019;179:1–10. https://doi.org/10.1016/j.solener.2018.12.048.
[13] Tsai DM, Wu SC, Li WC. Defect detection of solar cells in electroluminescence images using Fourier image reconstruction. Sol Energy Mater Sol Cells 2012;99: 250–62. https://doi.org/10.1016/j.solmat.2011.12.007.
[14] Koch S, Weber T, Sobottka C, Fladung A, Clemens P, Berghold J. Outdoor electroluminescence imaging of crystalline photovoltaic modules: comparative study between manual ground-level inspections and drone-based aerial surveys, 2016.
[15] Tsanakas JA, Ha LD, Al SF. Advanced inspection of photovoltaic installations by aerial triangulation and terrestrial georeferencing of thermal/visual imagery. Renew Energy 2017;102:224–33. https://doi.org/10.1016/j.renene.2016.10.046.
[16] Tsanakas JA, Chrysostomou D, Botsaris PN, Gasteratos A. Fault diagnosis of photovoltaic modules through image processing and Canny edge detection on field thermographic measurements. Int J Sustain Energy 2015;34(6):351–72. https://doi.org/10.1080/14786451.2013.826223.
[17] Jiang L, Su J, Li X, Hamouda SA, Mirzaei M, Yu Z. Hot Spots Detection of Operating PV Arrays through IR Thermal Image Using Method Based on Curve Fitting of Gray Histogram. MATEC Web Conf 2016;61:06017. https://doi.org/10.1051/matecconf/20166106017.
[18] Jaffery ZA, Dubey AK, Irshad, Haque A. Scheme for predictive fault diagnosis in photo-voltaic modules using thermal imaging. Infrared Phys Technol 2017;83: 182–7. https://doi.org/10.1016/j.infrared.2017.04.015.
[19] Kurukuru VSB, Haque A, Khan MA, Tripathy AK. Fault classification for Photovoltaic Modules Using Thermography and Machine Learning Techniques. 2019 Int. Conf. Comput. Inf. Sci. ICCIS 2019, Institute of Electrical and Electronics Engineers Inc.; 2019. https://doi.org/10.1109/ICCISci.2019.8716442.
[20] Costilla-Reyes O, Scully P, Ozanyan KB. Deep Neural Networks for Learning Spatio-Temporal Features From Tomography Sensors. IEEE Trans Ind Electron 2018;65 (1):645–53. https://doi.org/10.1109/TIE.2017.2716907.
[21] Zeng M, Nguyen LT, Yu B, Mengshoel OJ, Zhu J, Wu P, et al. Convolutional Neural Networks for human activity recognition using mobile sensors. Proc. 2014 6th Int. Conf. Mob. Comput. Appl. Serv. MobiCASE 2014, Institute of Electrical and Electronics Engineers Inc.; 2015, p. 197–205. https://doi.org/10.4108/icst.mobicase.2014.257786.
[22] Huerta Herraiz Á, Pliego Marugán A, García Márquez FP. Photovoltaic plant condition monitoring using thermal images analysis by convolutional neural network-based structure. Renew Energy 2020;153:334–48. https://doi.org/10.1016/j.renene.2020.01.148.
[23] Pierdicca R, Malinverni ES, Piccinini F, Paolanti M, Felicetti A, Zingaretti P. Deep convolutional neural network for automatic detection of damaged photovoltaic cells 2018. https://doi.org/10.5194/isprs-archives-XLII-2-893-2018.

[24] Cipriani G, D'Amico A, Guarino S, Manno D, Traverso M, Di Dio V. Convolutional Neural Network for Dust and Hotspot Classification in PV Modules. Energies 2020; 13:6357. https://doi.org/10.3390/en13236357.
[25] Abderrezek M, Fathi M. Experimental study of the dust effect on photovoltaic panels' energy yield. Sol Energy 2017;142:308–20. https://doi.org/10.1016/j.solener.2016.12.040.
[26] Zefri Y, ElKettani A, Sebari I, Lamallam SA. Thermal Infrared and Visual Inspection of Photovoltaic Installations by UAV Photogrammetry—Application Case: Morocco. Drones 2018;2:41. https://doi.org/10.3390/drones2040041.
[27] Carletti V, Greco A, Saggese A, Vento M. An intelligent flying system for automatic detection of faults in photovoltaic plants. J Ambient Intell Humaniz Comput 2020; 11(5):2027–40. https://doi.org/10.1007/s12652-019-01212-6.
[28] Addabbo P, Angrisano A, Bernardi ML, Gagliarde G, Mennella A, Nisi M, et al. A UAV infrared measurement approach for defect detection in photovoltaic plants. 4th IEEE Int. Work. Metrol. AeroSpace, Metroaerosp. 2017 - Proc., Institute of Electrical and Electronics Engineers Inc.; 2017, p. 345–50. https://doi.org/10.1109/MetroAeroSpace.2017.7999594.
[29] Kato K. PVRessQ!: a research activity on reliability of PV systems from an user's viewpoint in Japan. In: Dhere NG, Wohlgemuth JH, Lynn KW, editors. Reliab. Photovolt. Cells, Modul. Components, Syst. IV, vol. 8112, SPIE; 2011, p. 81120K. https://doi.org/10.1117/12.896135.
[30] Haque A, Bharath KVS, Khan MA, Khan I, Jaffery ZA. Fault diagnosis of Photovoltaic Modules. Energy Sci Eng 2019;7(3):622–44. https://doi.org/10.1002/ese3.255.
[31] Shin W, Ko S, Song H, Ju Y, Hwang H, Kang G. Origin of Bypass Diode Fault in c-Si Photovoltaic Modules: Leakage Current under High Surrounding Temperature. Energies 2018;11:2416. https://doi.org/10.3390/en11092416.
[32] Gallardo-Saavedra S, Hernández-Callejo L, Duque-Pérez Ó. Analysis and Characterization of Thermographic Defects at the PV Module Level. Commun. Comput. Inf. Sci., vol. 978, Springer Verlag; 2019, p. 80–93. https://doi.org/10.1007/978-3-030-12804-3_7.
[33] Gosumbonggot J, Fujita G. Global Maximum Power Point Tracking under Shading Condition and Hotspot Detection Algorithms for Photovoltaic Systems. Energies 2019;12:882. https://doi.org/10.3390/en12050882.
[34] Deng J, Dong W, Socher R, Li L-J, Li K. Li Fei-Fei. ImageNet: A large-scale hierarchical image database. Institute of Electrical and Electronics Engineers (IEEE) 2010:248–55. https://doi.org/10.1109/cvpr.2009.5206848.
[35] Li X, Yang Q, Lou Z, Yan W. Deep Learning Based Module Defect Analysis for Large-Scale Photovoltaic Farms. IEEE Trans Energy Convers 2019;34(1):520–9. https://doi.org/10.1109/TEC.2018.2873358.
[36] Gopalakrishnan K, Khaitan SK, Choudhary A, Agrawal A. Deep Convolutional Neural Networks with transfer learning for computer vision-based data-driven pavement distress detection. Constr Build Mater 2017;157:322–30. https://doi.org/10.1016/j.conbuildmat.2017.09.110.
[37] Rezende E, Ruppert G, Carvalho T, Theophilo A, Ramos F, de Geus P. Malicious Software Classification Using VGG16 Deep Neural Network's Bottleneck Features. Adv. Intell. Syst. Comput., vol. 738, Springer Verlag; 2018, p. 51–9. https://doi.org/10.1007/978-3-319-77028-4_9.
[38] López-Fernández L, Lagüela S, Fernández J, González-Aguilera D. remote sensing Automatic Evaluation of Photovoltaic Power Stations from High-Density RGB-T 3D Point Clouds 2017. https://doi.org/10.3390/rs9060631.
[39] Vidal De Oliveira AK, Madukanya UE, Rüther R. Fault inspection by aerial infrared thermography in a pv plant after a meteorological tsunami. vol. 10. 2019.
[40] Krishnaswamy Rangarajan A, Purushothaman R. Disease Classification in Eggplant Using Pre-trained VGG16 and MSVM. Sci Rep 2020;10:1–11. https://doi.org/10.1038/s41598-020-59108-x.
[41] Simonyan K, Zisserman A. Very deep convolutional networks for large-scale image recognition. 3rd Int. Conf. Learn. Represent. ICLR 2015 - Conf. Track Proc., International Conference on Learning Representations, ICLR; 2015.
[42] Kumar Reddy RV, Srinivasa Rao B, Raju KP. Handwritten Hindi Digits Recognition Using Convolutional Neural Network with RMSprop Optimization. Proc. 2nd Int. Conf. Intell. Comput. Control Syst. ICICCS 2018, Institute of Electrical and Electronics Engineers Inc.; 2019, p. 45–51. https://doi.org/10.1109/ICCONS.2018.8662969.
[43] Ketkar N. Convolutional Neural Networks. Deep Learn. with Python, Berkeley, CA: Apress; 2017, p. 63–78. https://doi.org/10.1007/978-1-4842-2766-4_5.
[44] Chieng HH, Wahid N, Ong P, Perla SRK. Flatten-T Swish: a thresholded ReLU-Swish-like activation function for deep learning. Int J Adv Intell Informatics 2018; 4:76–86. https://doi.org/10.26555/ijain.v4i2.249.
[45] Nwankpa C, Ijomah W, Gachagan A, Marshall S. Activation Functions: Comparison of trends in Practice and Research for Deep Learning. ArXiv 2018.
[46] Tao H, Lu X. On comparing six optimization algorithms for network-based wind speed forecasting. Chinese Control Conf. CCC, vol. 2018- July, IEEE Computer Society; 2018, p. 8843–50. https://doi.org/10.23919/ChiCC.2018.8482567.
[47] Kingma DP, Ba JL. Adam: A method for stochastic optimization. 3rd Int. Conf. Learn. Represent. ICLR 2015 - Conf. Track Proc., International Conference on Learning Representations, ICLR; 2015.
[48] Ioffe S, Szegedy C. Batch normalization: Accelerating deep network training by reducing internal covariate shift. 32nd Int. Conf. Mach. Learn. ICML 2015, vol. 1, International Machine Learning Society (IMLS); 2015, p. 448–56.
[49] Deng X, Liu Q, Deng Y, Mahadevan S. An improved method to construct basic probability assignment based on the confusion matrix for classification problem. Inf Sci (Ny) 2016;340–341:250–61. https://doi.org/10.1016/j.ins.2016.01.033.
[50] Zhang J, Zheng M, Nan J, Hu H, Yu N. A Novel Evaluation Metric for Deep Learning-Based Side Channel Analysis and Its Extended Application to Imbalanced Data. IACR Trans Cryptogr Hardw Embed Syst 2020;2020:73–96. https://doi.org/10.13154/tches.v2020.i3.73-96.
[51] Huang H, Xu H, Wang X, Silamu W. Maximum F1-score discriminative training criterion for automatic mispronunciation detection. IEEE/ACM Trans Audio Speech Lang Process 2015;23(4):787–97. https://doi.org/10.1109/TASLP.2015.2409733.
[52] Zheng L, Zhao Y, Wang S, Wang J, Tian Q. Good Practice in CNN Feature Transfer 2016.
[53] Wendlandt S, Drobisch A, Buseth T, Krauter S, Grunow P. Hot spot risk analysis on silicon cell modules 2010:4002–6.
[54] Dotenco S, Dalsass M, Winkler L, Wurzner T, Brabec C, Maier A, et al. Automatic detection and analysis of photovoltaic modules in aerial infrared imagery. 2016 IEEE Winter Conf. Appl. Comput. Vision, WACV 2016, Institute of Electrical and Electronics Engineers Inc.; 2016. https://doi.org/10.1109/WACV.2016.7477658.
[55] Wei S, Li X, Ding S, Yang Q, Yan W. Hotspots Infrared detection of photovoltaic modules based on Hough line transformation and Faster-RCNN approach. 2019 6th Int. Conf. Control. Decis. Inf. Technol. CoDIT 2019, Institute of Electrical and Electronics Engineers Inc.; 2019, p. 1209–14. https://doi.org/10.1109/CoDIT.2019.8820333.
[56] Huang Y, Ding W, Li H. Haze removal for UAV reconnaissance images using layered scattering model. Chinese J Aeronaut 2016;29(2):502–11. https://doi.org/10.1016/j.cja.2016.01.012.
[57] Nie J, Luo T, Li H. Automatic hotspots detection based on UAV infrared images for large-scale PV plant. Electron Lett 2020;56(19):993–5. https://doi.org/10.1049/el.2020.1542.